

Review

Micro-computed tomography for small animal imaging: Technological details

Hao Li, Hui Zhang*, Zhiwei Tang, Guangshu Hu

Department of Biomedical Engineering, Tsinghua University, Beijing 100084, China

Received 29 October 2007; received in revised form 23 November 2007; accepted 20 January 2008

Abstract

The high-resolution micro-computed tomography (micro-CT) system has now become an important tool for biological research. The micro-CT system enables a non-invasive inspection to screen anatomical changes in small animals. The promising advantages include high-spatial resolution, high sensitivity to bone and lung, short scan time and cost-effectiveness. The dose received by the small animal might be a critical concern in the research. In this article, the choice of the components, fundamental physical problems, the image reconstruction algorithm and the representative applications of micro-CT are summarized. Some results from our research group are also presented to show high-resolution images obtained by the micro-CT system.

© 2008 National Natural Science Foundation of China and Chinese Academy of Sciences. Published by Elsevier Limited and Science in China Press. All rights reserved.

Keywords: Micro-computed tomography; Small animal; X-ray

1. Introduction

Small animals, especially small rodents, have been widely used for developing animal models in biomedical and biological research. Non-invasive imaging technologies are recognized as useful tools to inspect small animal's anatomy, pathology and development. Up to now, many imaging technologies have been developed including micro-computed tomography (micro-CT) [1–6], magnetic resonance microscopy (MRM) [7–9], high-frequency ultrasound imaging [10], micro-positron emission tomography (micro-PET) [11], high-resolution single photon emission computed tomography (SPECT) [12], and optical imaging [13]. Among them, the micro-CT system is generally used to provide high-resolution anatomical images of small animals, while micro-PET, high-resolution SPECT and the optical imaging are used to acquire functional images with

relatively lower resolution. Compared with MRM, the micro-CT system is a cost-effective choice for many laboratories. In this review article, we will discuss the choice of the components, fundamental physical problems, the image reconstruction algorithm and representative applications in micro-CT imaging.

2. System description

2.1. Scanning geometry

Although some micro-CT systems use the hierarchy of the first-generation clinical CT, currently most micro-CT systems adopt the third-generation CT scanning structure, where the X-ray source and the detector array rotate synchronously with respect to the scanned animal [1,6]. The scanning geometry can be roughly classified into two categories: rotational bed and rotational gantry, as shown in Fig. 1(a) and (b), respectively. In the rotational bed design, the small animal rotates on the bed while the X-ray source and the detector stay still to acquire projection data from

* Corresponding author. Tel.: +86 10 62773000 3; fax: +86 10 62784568.
E-mail address: hzhang@tsinghua.edu.cn (H. Zhang).

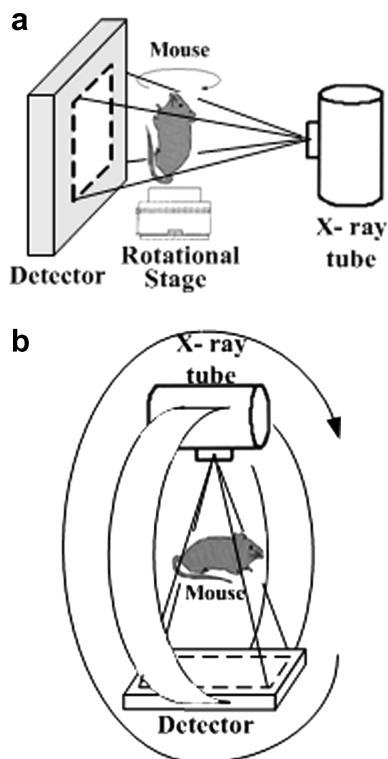


Fig. 1. Scanning geometry. (a) Rotational bed; (b) rotational gantry.

different angles. It is worthwhile to note that the small animal must be well confined in the rotating carrier to prevent soft tissue movement. In the rotational gantry design, the small animal lies in the fixed bed, while the X-ray source and the detector rotates around the subject, like clinical CT systems. The rotational gantry may usually guarantee a higher spatial resolution compared to the rotational bed design since the small animal can stay still and the soft tissue movement can be largely reduced during the long scan time, typically more than 5 min [1].

2.2. Basic components

2.2.1. X-ray tube

One critical part of the micro-CT system is the X-ray tube. Generally, the bench-top micro-CT systems use a microfocus X-ray tube, whose focal spot diameter is less than 100 μm , in order to resolve fine details in the scanned objects. Synchrotron-based systems, capable of much higher resolution [14,15], are not practical for most laboratories. When using the microfocus X-ray tube, it is worthy to note that a sufficiently large X-ray output should be provided by the tube to make sure that enough exposure can be delivered in a reasonable time, and satisfactory signal-to-noise ratio (SNR) can be achieved. The maximal power of the microfocus X-ray tube is often limited [16], namely

$$P_{\max} = 1.4(d)^{0.88} \quad (1)$$

where d represents the focal spot diameter of the tube in micrometer. That means, largely for an X-ray tube with a

50 μm focal spot, and the maximal power could be approximately not more than 45 W. The limitation of the tube is mainly due to the limitation of heat load capacity, thus a tradeoff has to be made between the focal spot size and the tube output when choosing an X-ray tube.

Once the X-ray tube has been chosen, the intensity of the emission X-ray beam emitted from the tube depends on the high voltage operated on the tube and the tube current. The number of X-ray photons emitted is proportional to the tube current, while the energy of the X-ray beam is proportional to the square of the accelerating voltage, thus the intensity I can be expressed as follows, neglecting the “heel effect” [17]:

$$I \propto (\text{kV})^2 (\text{mA}) \quad (2)$$

Recently, the carbon nanotube-based microfocus X-ray tubes have been developed for micro-CT [18–20]. The reported focal spot diameter is approximately 30 μm with a high-temporal resolution and stable emission. A high-spatial-temporal resolution of the carbon nanotube-based X-ray tube is attractive for dynamical tomography imaging.

2.2.2. X-ray detector

Conceptually, X-ray detectors convert the incident X-ray photons into collectable electrical charges and digitize them later. Image intensifiers (XRII) have been and are still used [5,21,22]. Since detectors have become more advanced, most commercially available micro-CT [1] and many laboratory micro-CT [23–26] systems utilize the charge coupled device (CCD) coupled to a phosphor screen via an optical lens or a fiber optic. Other types of detectors have also been reported, including hydrogenated amorphous silicon (a-Si:H) detectors [27,28], amorphous selenium (a-Se) [29] and CMOS image sensors [30–33].

The XRII seems to be the only dose-efficient X-ray instrument for fluoroscopy in real-time display [34]. The XRII absorbs the incident X-ray photons in the input phosphor screen, then the photoemissive layer, which is evaporated directly on the phosphor, radiates electrons. The emitted electrons are accelerated and focused, finally hit on the small output phosphor screen. The XRII greatly amplifies the brightness of the input image, however, due to its unavoidable distortion and other imperfectness, the calibration of the tomography system using XRII as the detector becomes a tough and time-consuming task.

The CCD was first developed in 1970 [35]. With the development of the extremely pure crystalline silicon manufacture and very large scale integration (VLSI), the CCD has gained very wide applications in digital imaging, mainly due to its superiority in high-spatial resolution, wide dynamic range and high linearity. The photoelectric absorption of optical quanta generates the charges within the semiconductor, then the charges are transferred and readout to form the signal. Usually, the CCD as the X-ray detector is coupled to the phosphor layer through the optical lens or the fiber optic. However, the coupling

procedure might cause large loss of energy and detection efficiency during the data acquisition.

The a-Si:H detector has been considered as a possible alternative among the flat panel detectors for the past two decades [36,37]. In the a-Si:H detector, X-ray photon interacts with the front scintillator layer, then the underlying a-Si:H detector matrix converts the light emitted by the scintillator into electrical signals. Typical scintillator layers used in the a-Si:H detector include gadolinium oxysulfides (e.g. $\text{Gd}_2\text{O}_2\text{S:Tb}$) and thallium-doped cesium iodide (CsI(Tl)).

Due to the high atomic number and density as well as the high resistivity, a-Se is used as the direct conversion of X-ray into electrical signals [38]. Unlike the phosphor-based system, where high-frequency image information might be lost due to light diffusion, the a-Se detector shows promising detail preservation even if the plate is made thick enough to absorb most incident X-ray photons. The a-Se layer attenuates the X-rays, generates free electron-hole pairs, and has collected them at the electrodes where the electric field is applied. The latent charge image is read out and forms a digital image. The main advantages of the a-Se detector include its high image quality, high real-time readout rate and its compact size.

An evaluation of the detector performance has been conducted between a-Se, a-Si and CCD detectors by Goertzen et al. [43]. They pointed out that the a-Se detector has high detective quantum efficiency (DQE), which is excellent for radiographic imaging. However, the sensitivity shift due to the exposure history makes it inappropriate for tomography application since tomography reconstruction requires a stable detector response. The CCD detector shows excellent stability relative to the a-Se detector; however, it has the worst modulation transfer function (MTF) characteristics among the three detectors, which is probably caused by the blurring in the phosphor layer as well as the optic fiber taper. The a-Si detector usually generates noisy images at low exposure levels since it has a large dark current component; but it has a good MTF because the detector array is directly coupled to the phosphor layer. The choice of phosphor layer seems have an important influence on the performance of the detector for a-Si and CCD. A CsI:Tl screen has a nearly doubled improvement in DQE compared to the $\text{Gd}_2\text{O}_2\text{S}$ screen, while the columnar structure of the CsI:Tl helps to offset the increased thickness of the screen to maintain the resolution. The image quality in the reconstructed image cannot be

predicted by DQE alone. The reconstructed images using the a-Se and a-Si detectors showed that the a-Si images appear with much less noise [43]. The reasons might be that though a-Si has a lower MTF, the smoothing effect implements a reduction of noise intrinsically.

Currently, the CMOS image sensors are becoming more competitive against CCD and are attracting more attention in the Micro-CT imaging. Compared with CCD, CMOS image sensors have many advantages including low power consumption, low cost, on-chip functionality, compatibility with standard CMOS technology, miniaturization, random access to image data, selective read-out mechanism, high-speed imaging and avoidance of blooming and smearing effects. Meanwhile, the disadvantages of the CMOS image sensors are low sensitivity, high noise, narrow dynamic range and unsatisfactory image quality [44].

The comparison for the five types of detectors is summarized in Table 1 for readers' quick reference. It can be found that there is no perfect detector for micro-CT imaging. Compromise should be made in the design according to the specific system requirements.

2.3. A prototype system

We have constructed a micro-CT system, which consists mainly of a micro-focus X-ray source, a high voltage power supply, a rotational stage with customized subject holder, a CMOS flat-panel detector and a host PC equipped with a National Instrument PCI-1422 frame grabber card [45]. The system adopts a rotational bed configuration in which the mouse rotates on the stage. The X-ray source used in the system is the XTF 5011 HP with a nominal focal spot of $47\ \mu\text{m}$ and a maximal power of 50 W, manufactured by Oxford Instruments, USA. The CMOS flat panel detector (C7921CA-02, Hamamatsu, Japan) was equipped to provide a detection area of $52.8\ \text{mm} \times 52.8\ \text{mm}$ with the pixel spacing of $50\ \mu\text{m}$. The micro-focus X-ray source continuously irradiates a subject, which is rotated in a step-by-step manner, and the CMOS flat-panel detector acquires a 2D projection image for each step, which is then input into the host PC for further image processing and 3D reconstructions. The host PC also maintains the overall system timing and provides synchronization between individual devices. It communicates with the high voltage power supply over Ethernet, and controls the rotational stage through a UART interface.

Table 1
Comparison of X-ray detectors

	XRII	CCD	a-Si	a-Se	CMOS
Advantage	Dose-efficient	High stability	High MTF	High DQE	Low power Low cost Compatibility
Disadvantage	Large distortion Narrow dynamic range	Low MTF	Noisy image at low exposure	Sensitivity shift	Large noise Low sensitivity

3. Physics of micro-CT

3.1. X-ray spectrum

The output of the X-ray tube consists of X-ray photons with a board range of energies, which are generated by either of the two mechanisms: bremsstrahlung radiation (general radiation) and characteristic radiation. The bremsstrahlung radiation mainly contributes to the continuous part in the X-ray spectrum, while the sharp peaks in the spectrum arise from the characteristic radiation. For the tungsten anode, there is no characteristic radiation below a 70 kV tube voltage.

Though the spectrum of X-ray tube is polychromatic, an effective or average X-ray energy can be given, which lies between one-third and one-half of the maximal X-ray photon energy, e.g. an X-ray tube operating at 150 kV has the emission X-ray energy for an effective value of approximately 68 keV. In imaging procedures, it is necessary to reduce the low-energy photons emitted from the tube via bremsstrahlung radiation by adding the filter because these X-ray photons cannot pass the object and reach the detector, and mainly contribute to the dose. Empirically, for a 50 kV tube voltage, 0.5 mm-thick aluminum filter is used; for a tube voltage between 50 and 70 kV, 1.5 mm-thick aluminum filter is used; and for a tube voltage above 70 kV, 2.5 mm-thick aluminum is used [17].

3.2. Spatial resolution

A number of measures have been used to describe the spatial resolution of micro-CT, e.g. the point spread function (PSF), the line spread function (LSF) and the edge spread function (ESF) in the spatial domain or the modulation transfer function (MTF) in the frequency domain.

MTF is an equivalent of the PSF in the spatial frequency domain. The MTF and PSF are closely related by:

$$\text{MTF}(k_x, k_y, k_z) = \int \int \int \text{PSF}(x, y, z) e^{-j2\pi k_x x} e^{-j2\pi k_y y} e^{-j2\pi k_z z} dx dy dz \quad (3)$$

where k_x , k_y and k_z are the spatial frequencies, in cycles/millimeter or line pairs/millimeter [17]. The spatial resolution can be denoted as the value at a specific position on the MTF curve, e.g. 10% MTF. An expression like 5LP/mm @ 10% MTF means that the spatial resolution of the system is approximately five line pairs per millimeter.

The measurement of the MTF, largely representing the system characteristics, can be implemented using the method provided by Boone [39], which is a direct extension of the method provided by Fujita et al. [40]. In Bonne's method, a simple phantom consisting of an aluminum foil sandwiched between the slabs is used. The aluminum foil is slightly angled with respect to the reconstruction matrix, and the CT images are acquired. An angled slit image is yielded to synthesize the LSF from which the MTF can be calculated.

3.3. CT number

The CT number is the traditional CT metric to measure the attenuation coefficient. The CT number in Hounsfield unit (HU) is calculated as

$$\text{CT number} = \frac{\mu - \mu_{\text{water}}}{\mu_{\text{water}}} \times 1000 \quad (4)$$

where μ_{water} and μ are the attenuation coefficients of water, and the tissue, respectively. It can be seen that the CT number of water is zero. The CT number of air, which has little attenuation of X-ray thus $\mu_{\text{air}} \approx 0$, is -1000 . The tissue that has a twice attenuation coefficient of water, such as bone, has a CT number of $+1000$. Most soft tissues have a CT number ranging from -100 to $+100$.

3.4. Optimal X-ray tube voltage

The X-ray data are typically Poisson-statistics limited. Grodzins [46] pointed out that the contrast resolution limit might be expressed as

$$\frac{\sigma_{\text{CT number}}}{\text{Measured CT number}} = \sqrt{\frac{2D \cdot \exp(\mu D)}{N(\Delta x)^3 \mu^2}} \quad (5)$$

where $\sigma_{\text{CT number}}$ is the standard deviation of the measured CT number, D the subject diameter, μ the attenuation coefficient, N the number of incident X-ray photons, and Δx the detector pixel sizing. Since the value of μ depends on the X-ray energy, different X-ray tube voltage has been tested to find out the optimal contrast resolution. Eq. (5) reaches the minimal value when $\mu = \frac{2}{D}$. For a 3 cm mouse-sized phantom, the optimal energy is approximately 25 keV. Since the X-ray spectrum is polychromatic, the aforementioned energy refers to the effective energy of the X-ray beam.

3.5. Radiation dose

One critical concern for in vivo micro-CT imaging is the radiation dose received by the small animal. In the literature [6,42], typical radiation doses were measured using small thermoluminescent dosimeters implanted into mice, and lie approximately in the range of 0.10–0.50 Gy. Being roughly 10% of typical LD50/30 (the dose that kills 50% of mice within 30 days of exposure, approximately 5 Gy), the cumulative dose for multiple scans within a single small animal over a period of time will be extremely high. Thus, the radiation-induced damage, immune response and apoptosis might be simultaneously observed after being scanned. However, animals that have been exposed to the dose of radiation at the level of 0.10–0.50 Gy might have very confusing biologic effects, even benefits sometimes. For example, non-obese diabetic mice received a single dose of 0.5 Gy showed suppressed progression of type I diabetes [41].

Therefore, it is critical and crucial to develop micro-CTs that would acquire high quality images under low radiation doses. Meanwhile, the radiation-induced effect should be taken much care of during the longitudinal research using micro-CT.

4. Image reconstruction

In image reconstruction, the signals received by the detector are first preprocessed to compensate for the imperfectness of the system, e.g. detector response heterogeneity, X-ray flux intensity drift, defective pixel correction, dark current subtraction and mechanical geometry calibration. After these steps, the corrected raw data are used for the reconstruction.

Many important categories of algorithms are used for the reconstruction, which include the Fourier-transform based backprojection algorithms [47–49] and statistical algorithms [50,51]. The most popular algorithm used in the micro-CT is the filtered backprojection (FBP). The first successful three-dimensional reconstruction algorithm for the cone-beam configuration is the Feldkamp–Davis–Kress (FDK) algorithm [52], which is an FBP and a non-exact algorithm. The FDK algorithm is widely used to implement the three-dimensional reconstruction in micro-CT [1] mainly due to its simplicity as well as the advantage in handling data truncation in the longitudinal direction.

The reconstruction in FDK is quite similar to the two-dimensional fan-beam FBP algorithm. In our reconstruction, we assumed that the data came from a planar detector, which is true in most cases for microtomography, and defined the projection angle β , the fan angle γ , the cone angle κ and the source trajectory radius R , as shown in Fig. 2. The figure also shows that a planar detector plane (a, b) is placed on the axis of rotation whose b -axis coincides with the z -axis. The data from the planar detector are placed in $p^F(\beta, a, b)$. In the first step, the data are pre-

weighted, and the convolution with the ramp-filter is applied on the pre-weighted data:

$$\tilde{p}^F(\beta, a, b) = \left(\frac{R}{\sqrt{R^2 + a^2 + b^2}} \cdot p^F(\beta, a, b) \right) * g^p(a) \tag{6}$$

The pre-weighting factor can be geometrically described as the product of two cosine factors of the fan angle and the cone angle as

$$\begin{aligned} \frac{R}{\sqrt{R^2 + a^2 + b^2}} &= \frac{R}{\sqrt{R^2 + a^2}} \frac{\sqrt{R^2 + a^2}}{\sqrt{R^2 + a^2 + b^2}} \\ &= \cos \gamma \cos \kappa \end{aligned} \tag{7}$$

Then the pre-weighted and filtered data are backprojected into the reconstructed voxels as

$$f_{\text{FDK}}(x, y, z) = \int_0^{2\pi} \frac{R^2}{U(x, y, \beta)^2} \tilde{p}^F(\beta, a(x, y, \beta), b(x, y, z, \beta)) d\beta \tag{8}$$

where

$$\begin{aligned} a(x, y, \beta) &= R \frac{-x \sin \beta + y \cos \beta}{R + x \cos \beta + y \sin \beta} \\ b(x, y, z, \beta) &= z \frac{R}{R + x \cos \beta + y \sin \beta} \end{aligned}$$

and

$$U(x, y, \beta) = R + x \cos \beta + y \sin \beta$$

The FDK algorithm is an approximate and non-exact method because it does not meet the Tuy-Smith sufficiency condition [53], which states that exact reconstruction is possible if all planes intersecting the object also intersect the source trajectory at least once. The reconstruction result will deviate somewhat from the measured object regardless of the measurement resolution. The algorithm is exact in the mid-plane, while for moderate cone angles, the deviation is small and often acceptable. For details of other cone-beam reconstruction algorithms using filtered backprojection, please refer to Ref. [54].

Since the computation needed for the cone-beam reconstruction is considerably large, many solutions have been proposed to reduce the reconstruction time. Efforts have been made on the algorithm, such as the divide-and-conquer method [55], the table-mapping method [56], and the distance-driven method [57]. The customized hardware is also used to achieve reduced reconstruction speed. The use of application specific integrated circuit (ASIC) largely reduces the reconstruction time but at the cost of limited algorithm flexibility, while the field-programmable gate array (FPGA)-based component is used to achieve more flexibility [58]. Distributing the computation across multiple PCs has been a popular solution in the past decade [59–62]. Recently, the accelerated texture mapping in the PC-based graphic boards is used as a cost-effective choice to accelerate the reconstruction process [63]. The combination of FPGA and graphic board seems a promising method in the reconstruction implementation in the future.

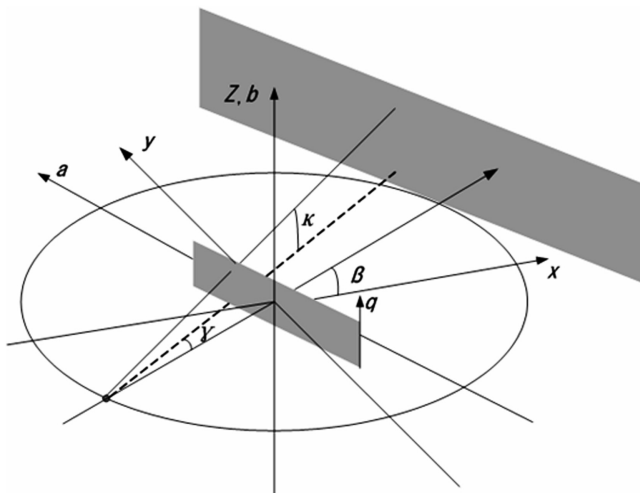


Fig. 2. Geometry description for the FDK algorithm.

5. Applications

In this section, the application of the micro-CT system is reviewed and described. Meanwhile, the result of our work is also presented as a representative application for readers' reference. The high-resolution scan and three-dimensional visualization of the system can be used for non-invasive imaging of different organ systems for preclinical research, including skeleton, chest, abdominal organs and brain. In multimodality imaging, the attenuation mapping provided by micro-CT could be used to aid the imaging of other modalities, such as SPECT.

5.1. Bone

One predominant application of micro-CT is to examine trabecular bone non-destructively. The large attenuation difference between the bone and soft tissue enables micro-CT to evaluate the bone cancellous structure. The micro-CT data are more informative and quantitative compared with 2D histological examination, which led to 3D measurements of trabecular bone morphology parameters such as trabecular thickness, spacing, density and connectivity [64–66]. Examples include the evaluation of osteoarthritis [67,68], bone metabolism [69,70] and gene-engineered mice skeleton [71].

5.2. Lung

Using micro-CT to investigate the mice pulmonary structure and function is limited by the low resolution, long scanning time and motion artifacts. Various technologies have been used to improve the performance of micro-CT lung imaging, e.g. respiratory gating [72–76], iso-pressure breath hold [77]. With these improved methodologies, there is growing interest to examine the anatomic and physiologic information for normal, acute or chronic diseased mice [73,75,78–80].

5.3. Vasculature

The primary means to study the structure of the vasculature structure has been by filling it with opaque materials such as India ink or polymers for study by light or scanning electron microscopy. However, methods like these might obscure deep vessels and provide little quantitative information. Having the vascular tissue filled or surrounded with a contrast agent, e.g. barium sulfate or lead chromate [81–83], micro-CT could be used to produce 3D images of vasculature structure at a spatial resolution typically less than 50 μm . Meanwhile, three-dimensional connectivity might be quantitatively investigated.

5.4. Multi-modality imaging

The multi-modality imaging which combines micro-CT with other imaging techniques such as micro-PET and micro-SPECT facilitates its use as an emerging tool for biological research. Several investigators have developed micro-PET/micro-CT suitable for small animal imaging [29]. The micro-PET can provide metabolic information of the tissue, while the information provided by the micro-CT helps to delineate the anatomical structure of the body and anatomical-functional relationship for further investigation. Also, a combined CT/SPECT system, which improved both the accuracy and the precision of *in vivo* radionuclide measurement, was developed [84]. Dual modality CT/SPECT allows for photon attenuation compensation since micro-CT provides the linear attenuation map of the scanned small animal. The correction might be evident when low-energy radionuclides are used, e.g. 30 keV for I-125 [85].

5.5. Results from our prototype system

With our developed system described in Section 2.3, the image data transferred from the frame grabber card were first preprocessed to operate dark current noise subtrac-

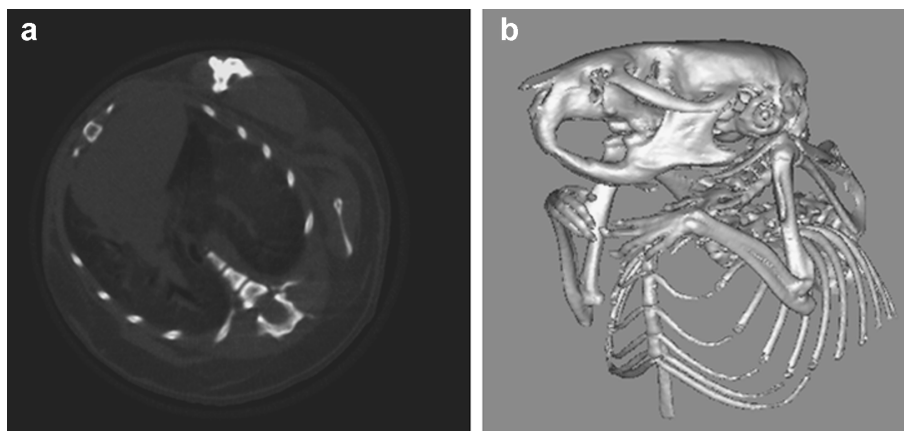


Fig. 3. Reconstruction results. (a) Transverse micro-CT image of the lung; (b) volume rendering of the skeletal dataset.

tion, flat field normalization and defective pixel correction. The system-dependent parameters for calibration, e.g. geometry calibration, were measured and stored on the host PC. An FDK algorithm was implemented to perform 3D reconstruction under the cone-beam geometry. Calibration was done to correct imperfectness of the system devices and to generate improved images with the artifact largely reduced. The reconstructed image of the mouse lung and volume rendering of the skeleton is shown in Fig. 3. It can be seen from the lung image that the lung and skeleton can be easily identified by the micro-CT. The soft tissue, e.g. subcutaneous fat layer and bronchus, can also be distinguished. Meanwhile, the contrast in bone and other tissue helps the excellent delineation of the skeleton structure, as shown in Fig. 3(b) [45]. Further system calibration and artifact reduction can be expected in future work.

6. Conclusion

Micro-CT imaging is now an important new tool to acquire quantitative 3D data for *in vivo* biological study. The main advantages of the micro-CT lie in the high-spatial resolution, sensitivity to skeleton and lung, and a low cost. However, its use is limited by the relatively poor contrast of soft tissue and by the radiation damage.

With the development of other modalities for small animal imaging, e.g. micro-PET, micro-CT system has been proved to be more valuable with the combination of other systems for biological research. The reciprocal role that micro-CT played in the combination such as providing the high-resolution image can largely benefit the imaging process for functional imaging. Newly invented system components such as the carbon nanotube-based microfocal X-ray tube and detectors with better performance can be introduced into the micro-CT design, which can further improve the system's capacity. The relatively low cost for X-ray imaging devices and board applications can enable the micro-CT a standard configuration method in research in the future.

Acknowledgement

This work was supported by National Program on Key Basic Research Project (Grant No. 2006CB705700).

References

- [1] Wang G, Vannier M. Micro-CT scanners for biomedical applications: an overview. *Adv Imaging* 2001;16:18–27.
- [2] Kujoori MA, Hillman BJ, Barrett H. High resolution computed tomography of the normal rat nephrogram. *Invest Radiol* 1980;15:148–54.
- [3] Sato T, Chieda O, Yamakashi Y, et al. X-ray tomography for microstructural objects. *Appl Opt* 1981;20:3880–3.
- [4] Burstein P, Bjorkholm PJ, Chase RC, et al. The largest and the smallest X-ray computed tomography systems. *Nucl Instrum Methods Phys Res* 1984;221:207–12.
- [5] Machin K, Webb S. Cone-beam X-ray microtomography of small specimens. *Phys Med Biol* 1994;39:1639–57.
- [6] Paulus MJ, Gleason SS, Kennel SJ, et al. High resolution X-ray computed tomography: an emerging tool for small animal cancer research. *Neoplasia* 2000;2(1–2):62–70.
- [7] Johnson GA, Thompson MB, Gewalt SL, et al. Nuclear magnetic resonance imaging at microscopic resolution. *J Magn Reson* 1986;68:129–37.
- [8] Eccles CD, Callaghan PT. High-resolution imaging: the NMR microscope. *J Magn Reson* 1986;68:393–8.
- [9] Jacobs RE, Ahrens ET, Meade TJ, et al. Looking deeper into vertebrate development. *Trends Cell Biol* 1999;9:73–6.
- [10] Pan L, Zan L, Foster FS. Ultrasonic and viscoelastic properties of skin under transverse mechanical stress *in vitro*. *Ultrasound Med Biol* 1998;24:995–1007.
- [11] Cherry SR, Shao Y, Silverman RW, et al. MicroPET: a high resolution PET scanner for imaging small animals. *IEEE Trans Nucl Sci* 1997;44:1161–6.
- [12] Weber DA, Ivanovic M, Franceschi D, et al. Pinhole SPECT: a new approach to *in vivo* high resolution SPECT imaging in small laboratory animals. *J Nucl Med* 1994;35:342–8.
- [13] Sharpe J, Ahlgren U, Perry P, et al. Optical projection tomography as a tool for 3D microscopy and gene expression studies. *Science* 2002;296:541–5.
- [14] Luo G, Kinney JH, Kaufman JJ, et al. Relationship between plain radiographic patterns and three-dimensional trabecular architecture in the human calcaneus. *Osteoporos Int* 1999;9:339–45.
- [15] Peyrin F, Salome M, Cloetens P, et al. Micro-CT examinations of trabecular bone samples at different resolutions: 14, 7 and 2 micron level. *Technol Health Care* 1998;6:391–401.
- [16] Flynn MJ, Hames SM, Reimann DA, et al. Microfocus X-ray sources for 3D microtomography. *Nucl Instrum Methods Phys Res A* 1994;352(1–3):312–5.
- [17] Webb A. Introduction to biomedical imaging. Hoboken: John Wiley & Sons, Inc.; 2003, 5–9, 220–224.
- [18] Liu Z, Zhang J, Yang G, et al. Development of a carbon nanotube based microfocus X-ray tube with single focusing electrode. *Rev Sci Instrum* 2006;77(5):054302–6.
- [19] Liu Z, Yang G, Lee YZ, et al. Carbon nanotube based microfocus field emission X-ray source for microcomputed tomography. *Appl Phys Lett* 2006;89(10):103111–3.
- [20] Zhang J, Cheng Y, Lee YZ, et al. A nanotube-based field emission X-ray source for microcomputed tomography. *Rev Sci Instrum* 2005;76(9):094301–4.
- [21] Holdsworth DW, Drangova M, Schulenburg KS, et al. Tabletop CT system for high-resolution volume imaging. *Proc Soc Photo Instrum Eng* 1990;1231:239–45.
- [22] Jenneson PM, Gilboy WB, Morton EJ, et al. An X-ray microtomography system optimised for the low-dose study of living organisms. *Appl Radiat Isot* 2003;58(2):177–81.
- [23] Paulus MJ, Sari-Sarraf H, Gleason SS, et al. A new X-ray computed tomography system for laboratory mouse imaging. *IEEE Trans Nucl Sci* 1999;46(3):558–64.
- [24] Cicalini E, Baldazzi G, Belcari N, et al. A high spatial resolution CT scanner for small animal imaging. *Nucl Phys B (Suppl)* 2006;150:313–6.
- [25] Song X, Frey EC, Tsui BMW. Development and evaluation of a MicroCT system for small animal imaging. *IEEE Nucl Sci Symp Conf Rec* 2001;3:1600–4.
- [26] Kastis GA, Furenlid LR, Wilson DW, et al. Compact CT/SPECT small-animal imaging system. *IEEE Trans Nucl Sci* 2004;51(1):63–7.
- [27] Jaffray DA, Siewerdsen JH. Cone-beam computed tomography with a flat-panel imager: initial performance characterization. *Med Phys* 2000;27(6):1311–23.
- [28] Khodaverdi M, Pauly F, Weber S, et al. Preliminary studies of a micro-CT for a combined small animal PET/CT scanner. *IEEE Nucl Sci Symp Conf Rec* 2001;3:1605–6.

- [29] Goertzen AL, Meadors AK, Silverman RW, et al. Simultaneous molecular and anatomical imaging of the mouse *in vivo*. *Phys Med Biol* 2002;47:4315–28.
- [30] Kim HK, Lee SC, Chun IK, et al. Performance evaluation of a flat-panel detector-based microtomography system for small-animal imaging. *IEEE Nucl Sci Symp Conf Rec* 2003;3:2108–13.
- [31] Lee SC, Kim HK, Chun IK, et al. A flat-panel detector based micro-CT system: performance evaluation for small-animal imaging. *Phys Med Biol* 2003;48:4173–85.
- [32] Kim HK, Lee SC, Cho MK, et al. Use of a flat-panel detector for microtomography: a feasibility study for small-animal imaging. *IEEE Trans Nucl Sci* 2005;52(1):193–8.
- [33] Domenico GD, Cesca N, Zavattini G, et al. CT with a CMOS flat panel detector integrated on the YAP-(S)PET scanner for *in vivo* small animal imaging. *Nucl Inst Meth in Phys Res Sec A* 2007;571(1–2):110–3.
- [34] Yaffe MJ, Rowlands JA. X-ray detectors for digital radiography. *Phys Med Biol* 1997;42:1–39.
- [35] Boyle WS, Smith GE. Charge-coupled semiconductor devices. *Bell Syst Tech J* 1970;49:587–93.
- [36] Piper W, Bigelow JE, Castleberry DE, et al. The demands on the a-Si FET as a pixel switch for liquid crystal displays. *Proc Soc Photo Instrum Eng* 1986;617:10–5.
- [37] Powell M. The physics of amorphous-silicon thin-film transistors. *IEEE Trans Elec Devi* 1989;36:2753–63.
- [38] Zhao W, Rowlands JA. X-ray imaging using amorphous selenium: feasibility of a flat panel self-scanned detector for digital radiology. *Med Phys* 1995;22:1595–605.
- [39] Boone JM. Determination of the presampled MTF in computed tomography. *Med Phys* 2000;28(3):356–60.
- [40] Fujita H, Tsai DY, Itoh T, et al. A simple method for determining the modulation transfer function in digital radiography. *IEEE Trans Med Imaging* 1992;11(1):34–9.
- [41] Takahashi M, Kojima S, Yamaoka K, et al. Prevention of type I diabetes by low-dose gamma irradiation in NOD mice. *Radiat Res* 2000;154(6):680–5.
- [42] Goertzen AL. Development of a combined microPET and microCT system for mouse imaging. PhD Dissertation. University of California, Los Angeles, USA, 2003.
- [43] Goertzen AL, Nagarkar V, Street RA, et al. A comparison of X-ray detectors for mouse CT imaging. *Phys Med Biol* 2004;49:5251–65.
- [44] Bigas M, Cabruja E, Forest J, et al. Review of CMOS image sensors. *Microelec J* 2006;37:433–51.
- [45] Zhang H, Li H, Hu G, et al. Micro-CT in a dual-modality fluorescence/computed tomography system for small animal imaging. In: *IEEE Nucl Sci Symp Conf Rec*, Honolulu, USA, October 28–November 3, 2007.
- [46] Grodzins L. Optimum energies for X-ray transmission tomography of small samples: applications of synchrotron radiation to computerized tomography. *Nucl Inst Meth* 1983;206:541–5.
- [47] Herman GT. Image reconstruction from projections: the fundamentals of computerized tomography. New York: Academic Press; 1980.
- [48] Kak AC, Slaney M. Principles of computerized tomographic imaging. New York: IEEE Press; 1988.
- [49] Shepp LA, Logan BF. The Fourier reconstruction of a head section. *IEEE Trans Nucl Sci* 1974;21:21–43.
- [50] Lange K, Carson RE. EM Reconstruction algorithms for emission and transmission tomography. *J Comput Assist Tomogr* 1984;8:306–16.
- [51] Ollinger JM. Maximum-likelihood reconstruction of transmission images in emission computed tomography via the EM algorithm. *IEEE Trans Image Process* 1994;13:89–101.
- [52] Feldkamp LA, Davis LC, Kress JW. Practical cone-beam algorithm. *J Opt Soc Am* 1984;1(6):612–9.
- [53] Tuy H. An inversion formula for cone-beam reconstructions. *SIAM J Appl Math* 1983;43:546–52.
- [54] Turbell H. Cone-beam reconstruction using filtered backprojection. Ph.D. Dissertation. Department Elec. Eng., Linköping University, Sweden, 2001.
- [55] Turbell H, Danielson PE. Fast Feldkamp reconstruction. In: *Proc. int. Mtg fully 3D image reconstruct radiol. nucl. med.* vol. 5, 1999, pp. 311–314.
- [56] Shih A, Wang G, Cheng PC. Fast algorithm for X-ray cone-beam microtomography. *Microsc Microanal* 2001;7:13–23.
- [57] De Man B, Basu S. Distance-driven projection and backprojection in three dimensions. *Phys Med Biol* 2004;49:2463–75.
- [58] Leiser M, Coric S, Miller E, et al. Parallel-beam backprojection: an FPGA implementation optimized for medical imaging. *J VLSI Sig Proces* 2005;39(3):295–311.
- [59] Reimann DA, Chaudhary V, Flynn MJ, et al. Cone beam tomography using MPI on heterogeneous workstation clusters. In: *Proc. 2nd MPI Developers Conf.*, 1996, 142–148.
- [60] Laurent C, Peyrin F, Chassery JM, et al. Parallel image reconstruction on MIMD computers for three-dimensional cone-beam tomography. *Parallel Comput* 1998;24:1461–79.
- [61] Gregor J, Gleason SS, Paulus MJ, et al. Fast Feldkamp reconstruction based on focus of attention and distributed computing. *Int J Imaging Syst Technol* 2002;12(6):229–34.
- [62] Brasse D, Humbert B, Mathelin C, et al. Towards an inline reconstruction architecture for micro-CT systems. *Phys Med Biol* 2005;50:5799–811.
- [63] Xu F, Mueller K. Accelerating popular tomographic reconstruction algorithms on commodity PC graphics hardware. *IEEE Trans Nucl Sci* 2005;52(3):654–63.
- [64] Feldkamp LA, Goldstein SA, Parfitt AM, et al. The direct examination of three-dimensional bone architecture *in vitro* by computed tomography. *J Bone Miner Res* 1989;4(1):3–11.
- [65] Kuhn JL, Goldstein SA, Feldkamp LA, et al. Evaluation of a microcomputed tomography system to study trabecular bone structure. *J Orthop Res* 1990;8(6):833–42.
- [66] Guldberg RE, Ballock RT, Boyan BD, et al. Analyzing bone, blood vessels, and biomaterials with microcomputed tomography. *IEEE Eng Med Biol Mag* 2003;22(5):77–83.
- [67] Patel V, Issever AS, Burghardt A, et al. MicroCT evaluation of normal and osteoarthritic bone structure in human knee specimens. *J Orthop Res* 2006;21(1):6–13.
- [68] Boyd SK, Müller R, Zernicke RF. Mechanical and architectural bone adaptation in early stage experimental osteoarthritis. *J Bone Miner Res* 2002;17(4):687–94.
- [69] Robling AG, Hinant FM, Burr DB, et al. Improved bone structure and strength after long-term mechanical loading is greatest if loading is separated into short bouts. *J Bone Miner Res* 2002;17(8):1545–54.
- [70] Mawatari T, Miura H, Higaki H, et al. Effect of vitamin K2 on three-dimensional trabecular microarchitecture in ovariectomized rats. *J Bone Miner Res* 2000;15(9):1810–7.
- [71] Turner CH, Hsieh YF, Müller R, et al. Genetic regulation of cortical and trabecular bone strength and microstructure in inbred strains of mice. *J Bone Miner Res* 2000;15(6):1126–31.
- [72] Badea C, Hedlund LW, Johnson GA. Micro-CT with respiratory and cardiac gating. *Med Phys* 2004;31(12):3324–9.
- [73] Cavanaugh D, Johnson E, Price RE, et al. *In vivo* respiratory-gated micro-CT imaging in small-animal oncology models. *Mol Imaging* 2004;3(1):55–62.
- [74] Walters EB, Panda K, Bankson JA, et al. Improved method of *in vivo* respiratory-gated micro-CT imaging. *Am J Physiol Heart Circ Physiol* 2004;49(17):4163–72.
- [75] Cody DD, Nelson CL, Bradley WM, et al. Murine lung tumor measurement using respiratory-gated micro-computed tomography. *Invest Radiol* 2005;40(5):263–9.
- [76] Ford NL, Nikolov HN, Norley CJ, et al. Prospective respiratory-gated micro-CT of free breathing rodents. *Med Phys* 2005;32(9):2888–98.
- [77] Namati E, Chon D, Thiesse J, et al. *In vivo* micro-CT lung imaging via a computer-controlled intermittent iso-pressure breath hold (IIBH) technique. *Phys Med Biol* 2006;51(23):6061–75.

- [78] De Clerck NM, Meurrens K, Weiler H, et al. High-resolution X-ray microtomography for the detection of lung tumors in living mice. *Neoplasia* 2004;6(4):374–9.
- [79] Postnov AA, Meurrens K, Weiler H, et al. *In vivo* assessment of emphysema in mice by high resolution X-ray microtomography. *J Microsc* 2000;220(1):70–5.
- [80] Karau KL, Johnson RH, Molthen RC, et al. Microfocal X-ray CT imaging and pulmonary arterial distensibility in excised rat lungs. *Am J Physiol Heart Circ Physiol* 2001;281(3):1447–57.
- [81] Garcia-Sanz A, Rodriguez-Barbero A, Bentley MD, et al. Three-dimensional microcomputed tomography of renal vasculature in rats. *Hypertension* 1998;31:440–4.
- [82] Jorgensen SM, Demirkaya O, Ritman EL. Three-dimensional imaging of vasculature and parenchyma in intact rodent organs with X-ray micro-CT. *Am J Physiol Heart Circ Physiol* 1998;275(3):1103–14.
- [83] Bentley MD, Ortiz MC, Ritman EL, et al. The use of microcomputed tomography to study microvasculature in small rodents. *Am J Physiol Regul Integr Comp Physiol* 2002;282(5):1267–79.
- [84] Weisenberger AG, Wojcik R, Bradley EL, et al. SPECT-CT system for small animal imaging. *IEEE Trans Nucl Sci* 2003;50(1):74–9.
- [85] Hasegawa BH, Iwata K, Wong KH, et al. Dual-modality imaging of function and physiology. *Acad Radiol* 2002;9(11):1305–21.